

Shape-based ultrasound tomography using a Born model with application to high intensity focused ultrasound therapy

Başak Ülker Karbeyaz^{a)}

Analogic Corporation, Peabody, Massachusetts 01960, USA

Eric L. Miller^{b)}

Department of Electrical and Computer Engineering, Tufts University, Medford, Massachusetts 02215, USA

Robin O. Cleveland^{c)}

Department of Aerospace and Mechanical Engineering, Boston University, Boston, Massachusetts 02115, USA

(Received 30 June 2007; revised 20 February 2008; accepted 21 February 2008)

A shape-based ultrasound tomography method is proposed to reconstruct ellipsoidal objects using a linearized scattering model. The method is motivated by the desire to detect the presence of lesions created by high intensity focused ultrasound (HIFU) in applications of cancer therapy. The computational size and limited view nature of the relevant three-dimensional inverse problem renders impractical the use of traditional pixel-based reconstruction methods. However, by employing a shape-based parametrization it is only necessary to estimate a small number of unknowns describing the geometry of the lesion, in this paper assumed to be ellipsoidal. The details of the shape-based nonlinear inversion method are provided. Results obtained from a commercial ultrasound scanner and a tissue phantom containing a HIFU-like lesion demonstrate the feasibility of the approach where a 20 mm × 5 mm × 6 mm ellipsoidal inclusion was detected with an accuracy of around 5%. © 2008 Acoustical Society of America. [DOI: 10.1121/1.2897045]

PACS number(s): 43.80.Sh, 43.20.Fn, 43.20.Rz, 43.20.Bi [TDM]

Pages: 2944–2956

I. INTRODUCTION

Motivated by the need to develop noninvasive methods for monitoring high intensity focused ultrasound (HIFU) treatment of cancer, we consider the problem of localizing and characterizing the structure of a penetrable ellipsoidal scatterer embedded into a lossy homogeneous medium given backscatter ultrasound data. We propose an inversion method based on a Born forward model that can be potentially used to characterize HIFU lesions based on changes in sound speed and attenuation from rf data collected using a standard ultrasound array.

Over the past 15 years, there has been a significant interest in the development and clinical evaluation of HIFU for therapeutic applications, in particular the treatment of cancer.^{1–10} HIFU uses focused ultrasound to raise the temperature of the target tissue to above 60 °C in 2 to 3 s, creating a lesion of order a few millimeters in size.^{11,12} For example ter Haar *et al.*¹³ reported that a 1.7 MHz transducer, which had a focal pressure of 6 MPa, created ellipsoidal-shaped lesions in beef liver that were about 20 mm long (in the direction of the HIFU beam) and 4 mm in diameter. Two major advantages of HIFU compared to the other tumor ablation techniques, e.g., radiation or cryogenic therapy, is that it uses nonionizing radiation and can generate tissue necrosis at depth with minimal impact on the surrounding tissues. One of the challenges required to make HIFU a practically

useful tool for clinical application is the need for guidance of the HIFU treatment. As this treatment method is noninvasive it is necessary that an imaging method be available to guide the treatment and ensure full necrosis of the region of interest.

The current state of the art to monitor the HIFU lesions is magnetic resonance imaging (MRI), which can monitor time-dependent temperature elevation.^{14–16} Despite the success of MRI as a tool for monitoring HIFU, it is a relatively expensive option and requires the development and use of specialized MRI-compatible HIFU hardware. Also patients with metal or electrical implants (e.g., pacemakers) are excluded from MRI. These issues motivate the use of diagnostic ultrasound for HIFU monitoring and guidance.

Ultrasound is sensitive to the acoustic properties of the tissue, specifically, the sound speed, acoustic absorption, and density. It is potentially suitable for HIFU guidance as it has been reported that HIFU treatments affect both the sound speed and the attenuation values of the tissue while forming lesions.^{17–22} The change in sound speed is less than 20 m/s (about 1%) and peaks at temperatures between 50 and 70 °C and then decreases with further increase in the temperature. In most cases the change is reported to be reversible. The attenuation coefficient significantly increases within the values ranging from 80% to 700% and the change is irreversible.²³

These effects have been employed previously in ultrasound-based monitoring of HIFU. For example Simon *et al.*²⁴ and Pernot *et al.*²⁵ were able to estimate the changes in the temperature from the sound speed measurements. However, because of the reversible nature of the sound

^{a)}Electronic mail: bkarbeyaz@analogic.com.

^{b)}Electronic mail: elmiller@ece.tufts.edu.

^{c)}Electronic mail: robinc@bu.edu.

speed, the lesion will not be visible using this method once the tissue cools. The change in the attenuation is irreversible, hence an imaging approach based on capturing the changes in the attenuation should be more robust. The attenuation in the necrosed tissue is much higher than that of the surrounding healthy tissue, hence, the tissue behind the HIFU lesion would appear slightly darker in standard B-scan images. Processing the B-scan data, Baker and Bamber,²⁶ Annad and Kaczowski,²⁷ and Zhong *et al.*²⁸ detected the changes in the ultrasound images behind the lesion.

Traditional medical ultrasound scanners employ beam-forming to generate two-dimensional images. These techniques have enjoyed a great deal of success both because of their inherent computational efficiency as well as the quality of the imagery they provide. Less common is the use of tomographic approaches for processing ultrasound data. In cases where an ultrasound system can fully encircle a region of interest then it is possible to employ tomographic approaches as a diagnostic tool^{29,30} or to detect HIFU lesions.³¹ However, in the body the breast is perhaps the only organ that provides this access and most applications of HIFU therapy yield imaging problems for which only backscatter data, as are typically acquired by commercial ultrasonic transducers, will be available. As such, one would not expect image-formation type methods to yield the same high resolution results as in Ref. 29–31. Moreover, the fast back-projection computational methods of Refs. 29 and 30 are no longer applicable so that one must employ a discretized physical model for the interaction of ultrasound with tissue leading to some rather formidable computational challenges.

In this paper, we develop and validate a shape-based inversion designed for limited view, ultrasound tomographic applications such as HIFU lesion characterization. In the development of the inverse problem we invoked the following assumptions:

- (1) The shape of the object is taken to be ellipsoidal.
- (2) A Born-type model is assumed for describing the scattering processes.
- (3) The medium in which the object is embedded is taken to be homogeneous and lossy.

Each of these assumptions has been made more as a matter of convenience to allow us to concentrate on the primary objectives of the paper, which is the formulation of a shape-based tomography problem and the validation of this idea using experimentally acquired data from an off-the-shelf transducer. We address the relevance and impact of these assumptions in the following paragraphs and discuss how they can be lifted in Sec. VI.

In terms of shape-based modeling, we note that there has been considerable work in the past decade on the use of such models as the basis for inverse processing. For example, the reconstructions of ellipsoids have been considered using low frequency acoustic and electromagnetic data.^{32–36} However these methods do not address to penetrable scatterers, assume low-frequency plane wave excitation, and rely on the fact that the scattering amplitude is known. Our own efforts consider the use of ellipsoids as models for problems in diffuse optical tomography,³⁷ another diffusive imaging-type

application, where an ellipsoidal model was employed to describe perturbations in optical absorption properties for a breast imaging application. The work in this paper build most closely on that of Ref. 38 in that here we also consider the estimation of the parameters modeling the shape of an ellipsoid. Here, though, we generalize the problem to the case where there are multiple physical properties that are of interest (sound velocity, absorption, and density) each of which can, in theory, be associated with its own ellipsoid. We also consider specifically the high frequency, ultrasound problem rather than the diffusive applications cited earlier.

The use of a Born model in this paper and the assumption of spatial homogeneity are both closely related. They are driven by the size of the problem we were addressing. As will be discussed in Sec. III, the computational size of the relevant three-dimensional (3D) ultrasound problem renders impractical the straightforward use of a full wave field model. Given that our objective was to provide initial validation of the inversion scheme we are proposing as well as the success in processing experimental data, as demonstrated in Sec. V C, we have elected to delay to the future the substantial investment in effort that would be required to develop a fully nonlinear inversion scheme.

II. FORWARD MODEL

A. Derivation of the scattered field

The propagation of time harmonic ultrasound through an inhomogeneous, lossy medium can be described by the following frequency domain wave equation:³⁹

$$\nabla^2 p(r, \omega) - \nabla \ln \rho(r) \nabla p(r, \omega) + k^2(r, \omega) p(r, \omega) = q(r, \omega), \quad (1)$$

where r is a point in three space, ω is the angular frequency, $p(r, \omega)$ is the pressure at r and ω , $\rho(r)$ is the density, $k(r, \omega)$ is the wave number, and $q(r, \omega)$ is the source that creates the acoustic disturbance in the medium. In dispersive attenuating media, $k(r, \omega)$ has the form: $k(r, \omega) = \omega/c(r, \omega) - j\alpha(r, \omega)$ where $c(r, \omega)$ is the dispersive speed of sound and $\alpha(r, \omega)$ is the frequency-dependent attenuation coefficient.

In most tissue, dispersion is weak and the attenuation follows a power law. The sound speed can then be expressed as $c(r, \omega) = c_b + c_p(r)$, where c_b is the background sound speed and $c_p(r)$ the spatially dependent perturbation. Similarly, $\alpha(r, \omega) = \alpha_b(\omega) + \alpha_p(r, \omega)$ where $\alpha_b(\omega) = \alpha_{bo}(\frac{\omega}{\omega_0})^n$ is the background attenuation (typically $1 < n < 1.5$ for soft tissue) and $\alpha_p(r, \omega) = \alpha_{po}(r)(\omega/\omega_0)^n$ the perturbation. The square of the wave number can then be expressed as

$$k^2(r, \omega) \approx \frac{\omega^2}{c_b^2} - j \frac{2\omega\alpha_b(\omega)}{c_b} - c_p(r) \left[\frac{2\omega^2}{c_b^3} \right] - \alpha_p(r, \omega) \times \left[j \frac{2\omega}{c_b} \right]. \quad (2)$$

This can be decomposed into a background term

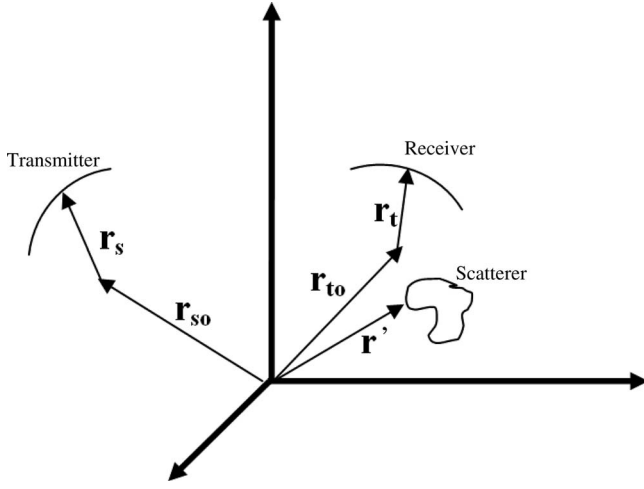


FIG. 1. Transmitter, receiver, and the scatterer location vectors.

$$k_b^2(\omega) = \frac{\omega^2}{c_b^2} - j \frac{2\omega\alpha_b(\omega)}{c_b} \quad (3a)$$

and a perturbation term

$$k_s^2(r, \omega) = c_p(r) \left[-\frac{2\omega^2}{c_b^3} \right] + \alpha_p(r, \omega) \left[-j \frac{2\omega}{c_b} \right], \quad (3b)$$

which is a *linear* function of scattering parameters.

We invoke the Born approximation to determine the scattered field in terms of the perturbation to the background properties:⁴⁰

$$p_s(r, \omega) = \int_{V'} G(r, r', \omega) k_s^2(r', \omega) p_b(r', \omega) d^3 r' - \int_{V'} G(r, r', \omega) \nabla \sigma_p(r') \cdot \nabla p_b(r', \omega) d^3 r', \quad (4a)$$

where $\sigma = \ln(\rho(r)) = \sigma_b + \sigma_p(r)$. After some algebraic manipulations the scattered field is given by⁴¹

$$p_s(r, \omega) = \int_{V'} \{ G(r, r', \omega) k_s^2(r', \omega) p_b(r', \omega) + \sigma_p(r') \cdot \nabla p_b(r', \omega) \cdot \nabla G(r, r', \omega) \} d^3 r', \quad (4b)$$

where $p_s(r, \omega)$ is the scattered field (i.e., the Fourier transform of the ultrasonic echoes), $p_b(r', \omega)$ is the background field; that is, the ultrasound field in the medium in the absence of the scatterer, $G(r, r', \omega)$ is the 3D free space lossy Green's function and V' is the boundary of the scattering volume.

B. Derivation of the measured pulse echo signal

Having presented the major equations, we now calculate the received signal, measured echo data, for a bistatic pulse-echo configuration.⁴² The configuration for the transmitter, receiver, and the scatterer locations is given in Fig. 1. The scatterer is identified by \mathbf{r}' and the origin of the transmitter and receiver coordinates are denoted by \mathbf{r}_{so} and \mathbf{r}_{to} , respec-

tively. The vectors that are traversing the surface of the transmitter and receiver transducers are given by \mathbf{r}_s and \mathbf{r}_t , respectively.

For this bistatic pulse-echo system the scattered field is given by

$$p_s(\mathbf{r}_{to} + \mathbf{r}_t, \omega) = \int_{V'} G(\mathbf{r}_{to} + \mathbf{r}_t, \mathbf{r}', \omega) \times (k_s^2(\mathbf{r}', \omega) p_b(\mathbf{r}', \mathbf{r}_{so}, \omega) - \nabla \sigma_p(\mathbf{r}') \cdot \nabla p_b(\mathbf{r}', \mathbf{r}_{so}, \omega)) d^3 \mathbf{r}, \quad (5)$$

where the background signal can be obtained from

$$p_b(\mathbf{r}', \mathbf{r}_{so}, \omega) = V_i(\omega) e_T(\omega) \int_S \frac{e^{-jk|\mathbf{r}' - (\mathbf{r}_s + \mathbf{r}_{so})|}}{4\pi|\mathbf{r}' - (\mathbf{r}_s + \mathbf{r}_{so})|} d^2 \mathbf{r}_s. \quad (6)$$

$V_i(\omega)$ is the Fourier transform of the uniform excitation voltage and $e_T(\omega)$ is the Fourier transform of the transmit electromechanical response of the transducer. The integral in Eq. (6) is the spatial transfer function and it relates the transducer geometry to the acoustic field.^{43–45} By means of this function, we can write

$$p_b(\mathbf{r}', \mathbf{r}_{so}, \omega) = V_i(\omega) e_T(\omega) H(\mathbf{r}', \mathbf{r}_{so}, \omega). \quad (7)$$

The received signal is the product of the scattered pressure field integrated over the receiver transducer surface and the electromechanical impulse response of the receiver, $e_R(\omega)$,

$$v_o(\mathbf{r}_{to}, \omega) = e_R(\omega) \int_S p_s(\mathbf{r}_{to} + \mathbf{r}_t, \omega) d^2 \mathbf{r}_t. \quad (8)$$

Using this definition and integrating Eq. (5) with respect to \mathbf{r}_t , one readily obtains

$$v_o(\mathbf{r}_{to}, \omega) = e_{pe}(\omega) \int_{V'} H(\mathbf{r}_{to}, \mathbf{r}', \omega) (k_s^2(\mathbf{r}', \omega) H(\mathbf{r}', \mathbf{r}_{so}, \omega) - \nabla \sigma_p(\mathbf{r}') \cdot \nabla H(\mathbf{r}', \mathbf{r}_{so}, \omega)) d^3 \mathbf{r}', \quad (9)$$

where $e_{pe}(\omega) = V_i(\omega) e_T(\omega) e_R(\omega)$. Finally using Green's theorem:

$$v_o(\mathbf{r}_{to}, \omega) = e_{pe}(\omega) \int_{V'} k_s^2(\mathbf{r}', \omega) H(\mathbf{r}_{to}, \mathbf{r}', \omega) H(\mathbf{r}', \mathbf{r}_{so}, \omega) d^3 \mathbf{r}' + e_{pe}(\omega) \int_{V'} \sigma_p(\mathbf{r}') \cdot \nabla H(\mathbf{r}_{to}, \mathbf{r}', \omega) \cdot \nabla H(\mathbf{r}', \mathbf{r}_{so}, \omega) d^3 \mathbf{r}'. \quad (10)$$

The primary characteristic of Eq. (10) is that it provides a linear relation between the measured backscatter data, $v_o(\mathbf{r}_{to}, \omega)$, and the medium parameters k_s^2 and σ_p .

III. INVERSION METHOD

The forward model for a medium with weak scatterers is obtained by substituting Eq. (3b) in Eq. (10) in which case

$$\begin{aligned}
v_o(\mathbf{r}_o, \omega) = & \int_{V'} K_1(r, r', \omega) c_p(r') d^3 r' \\
& + \int_{V'} K_2(r, r', \omega) \alpha_p(r') d^3 r' \\
& + \int_{V'} K_3(r, r', \omega) \sigma_p(r') d^3 r', \quad (11)
\end{aligned}$$

where K_i , $i=1,2,3$ depend only on the background properties. To represent the forward model for point sources, Eq. (4b) will be used to obtain K_i .

For the imaging system of interest in this work, it is assumed that multiple transmitters and receivers are used to obtain the measurements. For the case of N_T transmitters and N_R receivers with N_S frequency samples, the measured data \mathbf{y} can be written as a column vector of size $N_T \times N_S \times N_R$. Discretizing Eq. (11) at any position r' , the received echo voltage can be written in a matrix-vector model of the form:

$$\mathbf{y} = [\mathbf{K}_1 \mathbf{K}_2 \mathbf{K}_3] [\mathbf{f}_1^T \mathbf{f}_2^T \mathbf{f}_3^T]^T + \mathbf{n} = \mathbf{K} \mathbf{f} + \mathbf{n}, \quad (12)$$

where \mathbf{K} is the matrix representation of the integral; \mathbf{f}_1 is the column vector containing the voxel values of sound speed perturbation, c_p ; \mathbf{f}_2 is the column vector containing the voxel values of attenuation perturbation, α_p ; \mathbf{f}_3 is the column vector containing the voxel values of density perturbation, σ_p ; and \mathbf{n} is the additive sensor noise.

The ultimate goal is to estimate the unknown medium parameters \mathbf{f}_1 , \mathbf{f}_2 , and \mathbf{f}_3 , from measured backscatter data. One approach to this problem would be to use linear inversion methods, and try to reconstruct voxelated images of the sound speed, density, and absorption. The nominal wavelength for imaging in tissue is about 0.3 mm at 5 MHz and the physical size of the region to be imaged could be on order of 30 mm on a side. An accurate discretization of the problem, with a step of a tenth of a wavelength (0.03 mm), could require up to a billion voxels. The linear inversion problem is ill-posed for this case due to the large number of voxels defining each of the three unknown vectors \mathbf{f}_1 , \mathbf{f}_2 , \mathbf{f}_3 .

Our approach to the problem is based on the specification of the parameters describing the shape of the perturbations. We assume the shape of the perturbations is known, ellipsoids, but the locations, sizes, and orientations are unknown. Specifically, perturbations in Eq. (11), c_p , α_p , and σ_p , are represented by ellipsoidal shapes.

Therefore, to completely characterize the perturbation in one variable, we only need the location of the center, the lengths of the three axes of the ellipsoid, three angles that orient the ellipsoid in space, and contrast of the perturbation. Thus rather than having to invert for up to a billion voxels we have only $3 \times 10 = 30$ quantities to estimate from the measured data. In the case when c_p , α_p , and σ_p share the same geometry the number of unknowns reduces to 12. The inverse problem cast in this manner is therefore much better posed than the fully voxelated image.

A. Ellipsoid modeling

An ellipsoid can be defined mathematically with four elements:

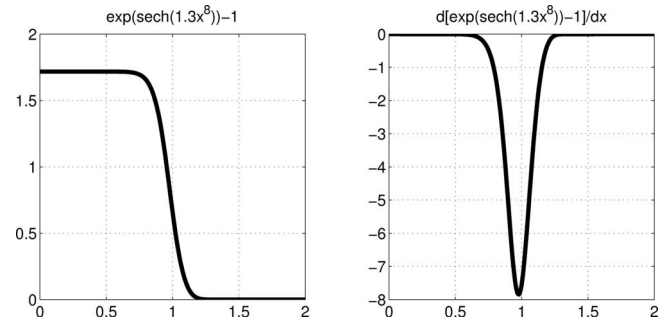


FIG. 2. The function $S(x) = \exp(\text{sech}(1.3x^8)) - 1$ and its derivative.

- (1) A length three vector, c , denoting the center of the ellipsoid, (x_o, y_o, z_o) .
- (2) A diagonal matrix $D = \text{Diag}(d)$ whose diagonal entries are inverses of the semiaxes lengths, (l_1, l_2, l_3) .
- (3) An orthonormal matrix U defining the ellipse in 3D using three Euler angles, $(\theta_1, \theta_2, \theta_3)$.
- (4) A constant M , defining the contrast of the object.

A point $r' = [x', y', z']^T$ is determined to be on or in the ellipsoid if

$$\|DU^T(r' - c)\|_2^2 \leq 1. \quad (13)$$

Hence, the ellipsoidal perturbations can be defined as

$$\gamma(r') = MS(1 - \|DU^T(r' - c)\|_2^2) = \begin{cases} M & r' \in \text{ellipsoid} \\ 0 & \text{otherwise} \end{cases}. \quad (14)$$

For an infinitely sharp interface $S(x)$ could be a step function. However, the step function model of the ellipsoid gives a discontinuity at the boundary of the ellipsoid. For purposes of inversion, where we wish to use gradient descent type methods to estimate the parameters of interest, we employ a smooth, analytical approximation to the step function as is common in many geometric-type processing methods.⁴⁶ It is more computationally efficient to have an analytical representation of the Jacobian which motivates choosing a differentiable expression that maps the parameters describing the shape to any point r' in the region of interest. Here the step function is approximated with a hyperbolic secant, see Fig. 2, and define the perturbations as

$$\gamma(r') = \exp(\tilde{M} \text{sech}(1.3\|DU^T(r' - c)\|_2^{16})) - 1. \quad (15)$$

The coefficient 1.3 is chosen so that without the scaling from the exponential function, the boundary value of the shape is set to 0.5 (the mean value of the change in the boundary).

If a point r_1 is within the ellipsoid, $\|DU^T(r_1 - c)\|_2^2$ is less than 1 and the value of $\gamma(r_1)$ approaches a constant value $[\exp(\tilde{M}) - 1]$. On the other hand, if r_1 is not within the ellipsoid, the value of Eq. (13) is larger than 1 and $\gamma(r_1)$ approaches 0. Around the boundary, the function provides a transition from 1 to 0. Therefore the expression approximates a step function, and classifies the points in the region of interest.

Our use of the hyperbolic secant function was motivated not by a desire to represent the transition from lesion to

healthy tissue, but rather as a mathematical convenience for use with the optimization method we use. With respect to the boundary in the tissue, there are data that indicate that the transition from necrosed to healthy tissue is very sharp—on the order of tens of cells.^{47,48} Relative to the ultrasonic wavelength the exact nature of the discontinuity is not resolvable and therefore could be represented by any number of functions. For the inversion, it was necessary to have differentiable functions and for that purpose we chose the sech function. We tested other functions to represent the sharp boundary, including arctan and arctanh, and found that the sech function provided marginally better results over the full range of experiments considered in the paper.

B. Inverse problem

The parameters that will be used to characterize the ellipsoids of the three acoustic properties will be

$$\beta_i = [x_{oi}, y_{oi}, z_{oi}, l_{1i}, l_{2i}, l_{3i}, \theta_{1i}, \theta_{2i}, \theta_{3i}, M_i],$$

where the subscripts $i=c, a, d$ will be used to represent the perturbations in sound speed, attenuation, and density, respectively. The representation of the perturbations given in Eq. (15a), $\gamma(r')$, will be replaced by $\gamma_i(r', \beta_i)$ to account for the parameters of each individual ellipsoid, where

$$\gamma_i(r', \beta_i) = \exp(\tilde{M}_i \operatorname{sech}(1.3 \|D_i U_i^T(r' - c_i)\|_2^{16})) - 1. \quad (16)$$

The problem to be solved given data \mathbf{y} , is the nonlinear least squares problem:

$$\min_{\beta_c, \beta_a, \beta_d} \|\mathbf{y} - \mathbf{Kf}(\beta)\|_2^2 \quad (17a)$$

$$\beta = \begin{bmatrix} \beta_c \\ \beta_a \\ \beta_d \end{bmatrix} \quad (17b)$$

In this work the minimization problem in Eq. (17a) was solved using the Gauss–Newton method.⁴⁹ For this purpose, an initial guess is provided for the ellipsoid parameters (β^0). Subsequent guesses (β^k) for the parameter vectors are then produced by the recurrence relation:

$$\beta^{k+1} = \beta^k + \alpha^k t^k, \quad (18)$$

where α^k is the sense optimal and t^k is the search direction obtained from the solution of

$$(J^T J) t^k = -J^T \|\mathbf{y} - \mathbf{Kf}(\beta^k)\|_2, \quad (19)$$

where J is the Jacobian. The computation of the Jacobian matrix is given in the Appendix. The search algorithm iterates until a termination tolerance is satisfied which is described in Sec. V.

IV. APPLICATION TO HIFU LESIONS

The equations presented in Sec. II A can be used to express the measured backscatter data from a lesion embedded in a weakly scattering medium as follows. The use of the Born approximation requires that the incident field is negligibly impacted by the presence of the lesion. In the case of HIFU lesions, the change in sound speed due to heating is

less than 1%, which is within the Born approximation. The attenuation coefficient increase by 80%–700% appears large but the constraint on the attenuation is defined as the smallness of α_p/k_b . The nominal attenuation in human tissue is 35.6 Np/m at 3.5 MHz. For the sound speed of 1551 m/s and 700% perturbation in attenuation, the ratio of α_p/k_b is 1.7% also within the Born approximation. Although our model accounts for changes in the density of tissue, the link between density and HIFU lesions has not yet been established. However, the density perturbations are included here for the completeness of the model. We were not able to identify measurements of density change in response to HIFU and therefore in this work the change in the density was limited to 1% to validate the Born model.

The applicability of the inversion method described in Sec. III to HIFU lesions is based on the fact that in HIFU there is substantial prior information about the target. The approximate size, location, and orientation of the lesion can be determined from the parameters of the HIFU source. In this work we will assume that the lesions are ellipsoidal in shape which is a reasonable model for purely thermal lesions.

We note that, after several excitations, the heated area may well lose its initial simple, ellipsoidal shape. Also, the morphology of the necrosed region may depend upon how the tissue is ablated, i.e., how the beam is scanned across the region of interest, and at what repetition rate. Depending upon these, the shape of the necrosed area may be quite arbitrary. However, the paradigm we introduce in this work can be extended to other shapes and this is addressed in the discussion.

V. INVERSION EXAMPLES AND RESULTS

In this section, the 3D shape-based inversion results for ellipsoidal Born scatterers are presented. In Sec. V A, the transducers are assumed to be point sources where the scattered field is represented by Eq. (4b) and in Sec. V B, a Monte Carlo analysis is done to determine the robustness of the inversion. In Sec. V C the proposed method is validated with measured ultrasound backscatter data from an ellipsoidal target that mimics a HIFU lesion. In this case the scattered field is represented by Eq. (10). In both cases the model given by Eq. (16) is used for the lesion structure and the contrast of the ellipsoidal-shaped perturbations in sound speed, attenuation, and density are estimated.

A. Numerical simulations and results

Here we present the numerical simulations that were used to validate the inversion idea on a problem of manageable size while the laboratory experiments presented in Sec. V C were dictated by the underlying, motivating application as well as the fact that the 3.5 MHz transducer is what is readily available in practice. In what follows we will employ a Monte Carlo approach to determine the behavior of the inversion and therefore to reduce the computational complexity for the numerical simulations, frequency values lower than those employed in the medical imaging applications were used, and the overall size of the problem was

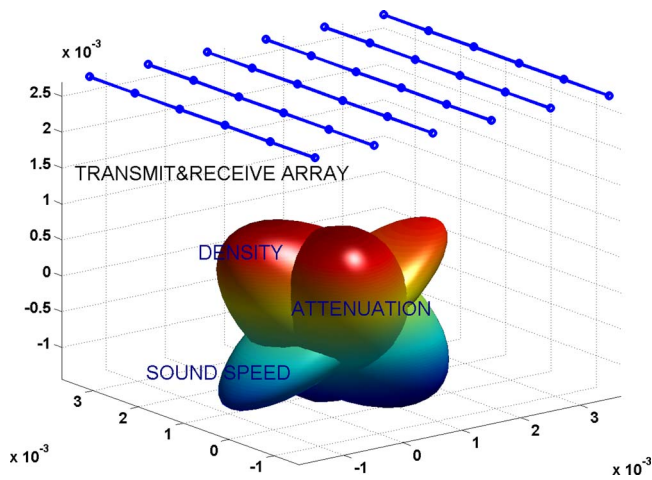


FIG. 3. (Color online) Setup for the numerical simulation showing three noncongruent perturbations. The connected dots show the six locations of the six element array that was used to detect the lesions.

reduced to $5 \text{ mm} \times 5 \text{ mm} \times 5 \text{ mm}$. Exploring ideas such as our ability to recover one ellipsoid per physical quantity could not be done easily at higher frequencies due to the long computational time associated with the size of the matrices for the high frequency case.

To demonstrate the flexibility of the shape-based approach three numerical simulation experiments were performed. Two cases were presented where three different ellipsoids were assumed for three different acoustic parameters and another case in which the spatial changes in the acoustic properties were represented by three overlapping ellipsoids (i.e., single ellipsoid). In practice, and indeed in the laboratory experiments, we assume a single ellipsoid in which the spatial changes in acoustic properties were enclosed within a single ellipsoid.

The numerical simulation conditions are given in Fig. 3. A linear array of six point sources are scanned across the anomaly at six different measurement points. At each measurement point, a single transmitter insonifies the medium where the echo data are calculated for each element of the array. Six frequencies equally spaced between 300 and 425 kHz were used in the simulations. Gaussian noise was added to the data to set the signal to noise ratio to 25 dB. The background properties were chosen to match those of a tissue mimicking phantom that we have employed previously:⁴¹ $c_b = 1551 \text{ m/s}$, $\rho_b = 1045 \text{ kg/m}^3$, $\alpha_b = 3.6 \text{ Np/m}$ (ω/ω_o)^{1.2} where $\omega_o = 2\pi 350 \text{ kHz}$. The values of the contrasts for a realistic problem were chosen as explained in the following. The total number of voxels in the region of interest was 4096 ($16 \times 16 \times 16$). The discretization step in terms of the smallest wavelength was one-tenth of a wavelength.

The bounds for the contrasts, M_i , were chosen as follows:

- (1) $0 \text{ m/s} < M_c < 20 \text{ m/s}$.
- (2) $0 \text{ Np/m} < M_a < 20 \text{ Np/m}$.
- (3) $0 \text{ kg/m}^3 < \sigma_p < 10 \text{ kg/m}^3$, hence $0 < M_d < 9.5 \times 10^{-3}$.

The inversion method described in Sec. III B was implemented in MATLAB where the “lsqnonlin” function with

TABLE I. Lower and upper limits for the geometric parameters of the ellipsoid.

	Lower limit	Upper limit
x_o	-2.5 mm	2.5 mm
y_o	-2.5 mm	2.5 mm
z_o	-2.5 mm	2.5 mm
l_1	$0.5 \mu\text{m}$	2.5 mm
l_2	$0.5 \mu\text{m}$	2.5 mm
l_3	$0.5 \mu\text{m}$	2.5 mm
θ_1	0	2π
θ_2	0	π
θ_3	0	2π

Gauss–Newton option was used. The geometric parameters and the contrasts of the ellipsoids, β_i were scaled to the same order (between 1 and 2) prior to the optimization routine to maximize the performance. The bounds for the geometric parameters are given in Table I. The lower limits for the lengths of the semiaxes were set to a small number ($0.5 \mu\text{m}$) to prevent the solution producing zero volume ellipsoids.

The lower and the upper bounds for the “lsqnonlin” function were set to 1 and 2, respectively, to ensure that the boundary of the ellipsoid was in the region of interest and the contrasts were within the above-defined limits. The termination tolerance on the function value, $\mathbf{y} - \mathbf{Kf}(\beta^k)$, was 10^{-5} .

In Figs. 4–6 the true and estimated ellipsoid distributions are displayed. For comparison purposes, the true shapes are plotted with lines on the estimated ellipsoids. Two measures are introduced to describe the error between the real and simulated ellipsoids. The estimation error in contrast is defined as

$$E_c \% = 100 \left| \frac{M_i - \bar{M}_i}{M_i} \right|, \quad (20)$$

where M_i and \bar{M}_i represent the actual and estimated contrasts, respectively. The volumetric estimation error is defined as

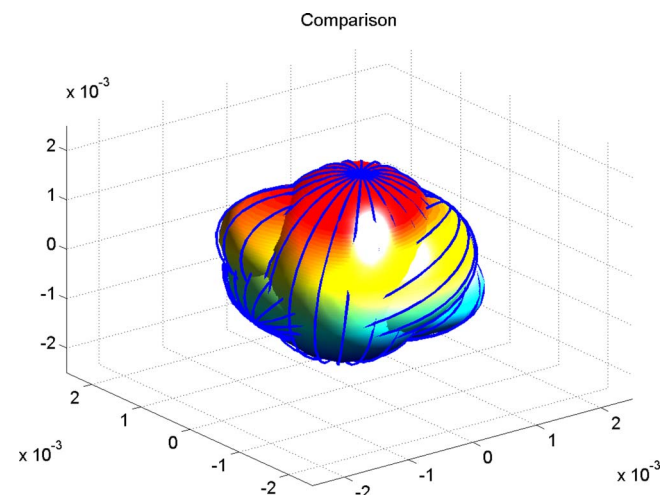


FIG. 4. (Color online) Case 1: Inversion for similarly sized and shaped ellipsoids.

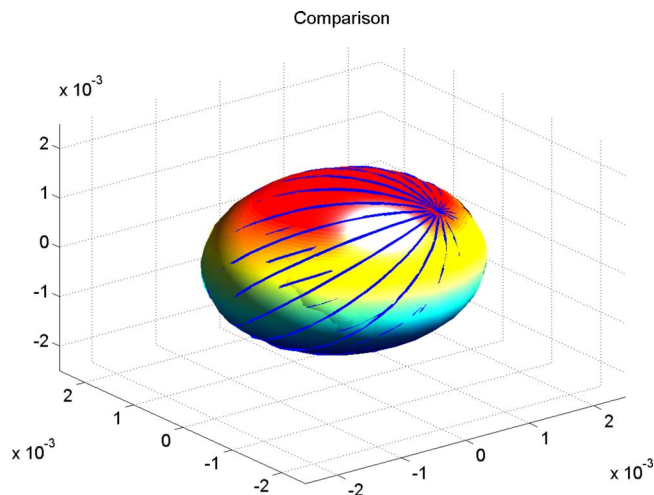


FIG. 5. (Color online) Case 2: Inversion for concentric and overlapping ellipsoids.

$$E_v \% = 100 \left(1 - \frac{\text{Volume}(E_a \cap E_e)}{\text{Volume}(E_a \cup E_e)} \right), \quad (21)$$

where E_a and E_e represent the actual and estimated ellipsoids, respectively. For comparison purposes, the real, initial, and estimated contrast values for all the simulations are given in Table II with the error values.

Figure 4 shows a case where the inclusion consists of similarly sized and shaped ellipsoids with different orientations. Given little prior information about the shape and the contrasts it was possible to recover the geometry and the contrasts quite accurately, with all errors less than 4%. The number of required iterations was 99, which took 14 min on a 1 GHz Linux workstation.

Figure 5 shows the HIFU lesion type anomaly where the inclusion consists of three concentric, overlapping ellipsoids. This represents the case of HIFU lesion where the changes of the acoustic properties are confined into a single region of space rather than individual ellipsoids. Although it appears that a single ellipsoid anomaly has been detected, the algorithm classified three distinct ellipsoids. Although the initial estimates for the contrasts were considerably different than the real values, a very good estimate was obtained for the contrasts and the geometries. The method proposed here to define the contrast of the object as a nonlinear parameter of

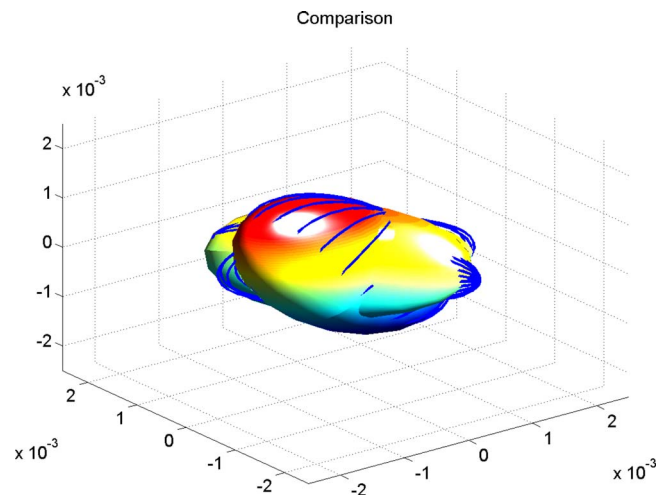


FIG. 6. (Color online) Case 3: Inversion for significantly different ellipsoids.

the problem, greatly improved the contrast detection. The number of required iterations was 98, which took 14 min on a 1 GHz Linux workstation.

In the third case, Fig. 6, the scenario consisted of three significantly different ellipsoids. Although this does not model what we expect to observe in a HIFU application it demonstrates the utility of the approach to a wider class of problems. The localization of the perturbations was successful although the differences were larger than for the other two cases. Our observations revealed that the rotation angles are the most difficult parameters to estimate for this type of shape-based inversion problem. The number of required iterations was 299, which took 24 min on a 1 GHz Linux workstation. The same experiment was repeated with signal-to-noise ratio of 40 dB and a better localization was obtained for the anomaly where the errors were less than 5%.

B. Monte Carlo analysis

A statistical error analysis was done to assess more thoroughly the performance of the inversion method presented in this study. For this purpose, Monte Carlo simulations were performed in which 140 estimation problems were considered. For each realization, a randomly oriented ellipsoid was selected so that it had up to 15% deviation in contrast, volume, and orientation from an *a priori* ellipsoid. Gaussian

TABLE II. Contrast and error values for the sound speed, attenuation, and density.

		Real	Initial	Estimate	E_c %	E_v %
Case 1	Speed (m/s)	3.58	20.00	3.71	3.59	3.00
	Density (kg/m ³)	4.99	10.00	4.87	2.32	2.05
	Attenuation (Np/m)	3.58	20.00	3.63	1.20	2.69
Case 2	Speed (m/s)	7.42	20.00	7.50	0.95	3.19
	Density (kg/m ³)	9.01	10.00	8.93	0.87	5.73
	Attenuation (Np/m)	7.42	20.00	8.16	9.88	2.26
Case 3	Speed (m/s)	13.57	20.00	10.52	22.01	32.94
	Density (kg/m ³)	10.00	10.00	10.00	0	1.41
	Attenuation (Np/m)	12.30	19.00	5.92	51.01	1.89

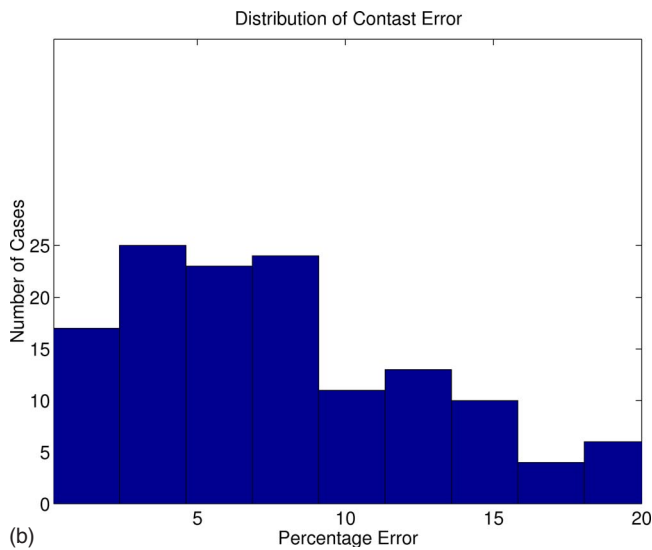
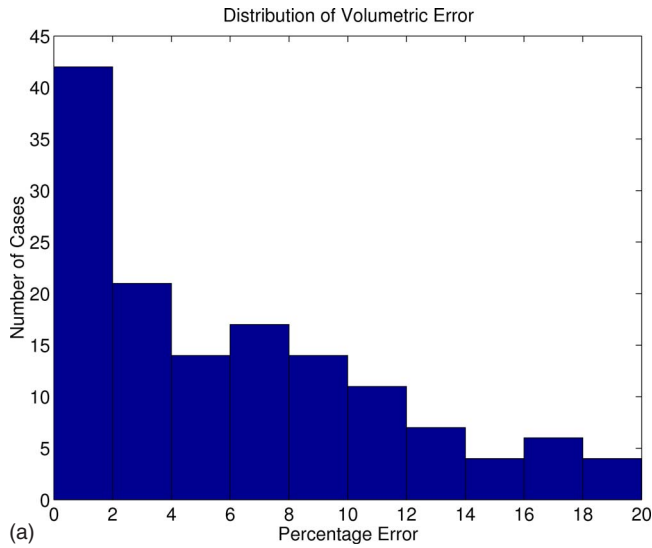


FIG. 7. (Color online) Distribution of volumetric (a) and contrast (b) errors. The total number of reconstructions was 140.

noise was added to the data to set the signal to noise ratio to 25 dB. The error distributions in volume and contrast are given in Fig. 7.

The algorithm was successful in localizing the ellipsoidal shapes but the performance was slightly poorer for contrast estimation. In 75% of the cases the localization error was less than or equal to 10%. For the problem of determining HIFU lesion position, the localization is more important than the contrast errors. On the other hand, the contrast estimation provides a means to construct a “safety zone” by which one can be assured that the tissue has in fact been necrosed. For all the cases where the error was high, the rotation parameters were significantly different (22%) than the actual values. This is consistent with the previous observation that the rotation parameters are the most difficult parameters to estimate.

The results showed that the method given in this study was generally successful in estimating the randomly oriented ellipsoids.

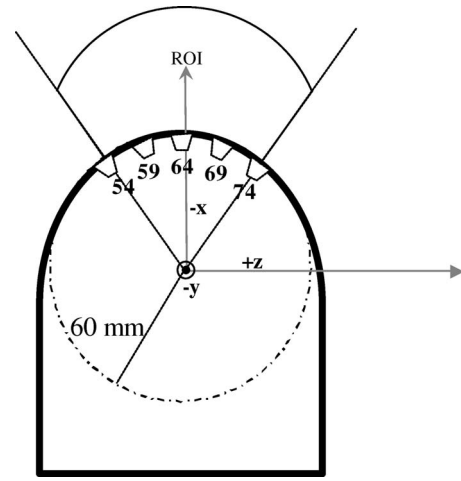


FIG. 8. Schematic of the locations of the transducers on the transducer array.

C. Laboratory experiment and results

A laboratory experiment with a clinical ultrasound transducer was performed to validate the inversion method developed in this paper. The probe (Model 8665, BK Medical, Wilmington, MA) was a curvilinear array with a 60 mm radius of curvature convex surface upon which 128 elements (13 mm high \times 0.5 mm wide) were placed with a pitch of 0.525 mm. Each element had a center frequency of 3.5 MHz and in the elevation plane was focused to 70 mm. Each element could be individually controlled using a real time ultrasound scanner (AN2300, Analogic Corporation, Peabody MA) with a MATLAB interface.

For this experiment five elements, Nos. 54, 59, 64, 69, and 74, were employed to take the measurements. The angle between each element used in this study was 0.0438 rad. The schematic showing the location of the cylindrically concave transducers on the linear array is given in Fig. 8.

The array transducer and the phantom were placed in a water tank (35 cm \times 53 cm \times 35 cm) that was filled with de-ionized, degassed water at approximately 21 °C. Each cylindrically concave element was operated in transmit mode individually and the unbeamformed echo data from other elements in the array were recorded and stored for post processing.

The laboratory experiment settings are given in Fig. 9. The origin of the region of interest (ROI) was defined as the geometric focus of the 64th element. The linear array was scanned across the ellipsoid anomaly at five different measurement locations. At each measurement location, a single element insonified the medium and the backscattered signal was measured by all five elements of the array. This was repeated using all elements of the array as a transmitter. The array was scanned across the anomaly between $y = -6$ mm to $y = 6$ mm with 3 mm step size.

An ellipsoidal shaped phantom (20 mm \times 5 mm \times 6 mm) was carved from an agar tissue mimicking phantom which had the nominal acoustic properties of $c_p = 1551$ m/s, $\rho_p = 1045$ kg/m³, and $\alpha_p = 10.17$ Np/m/MHz. The ellipsoid was immersed into a polyacrylamide hydrogel

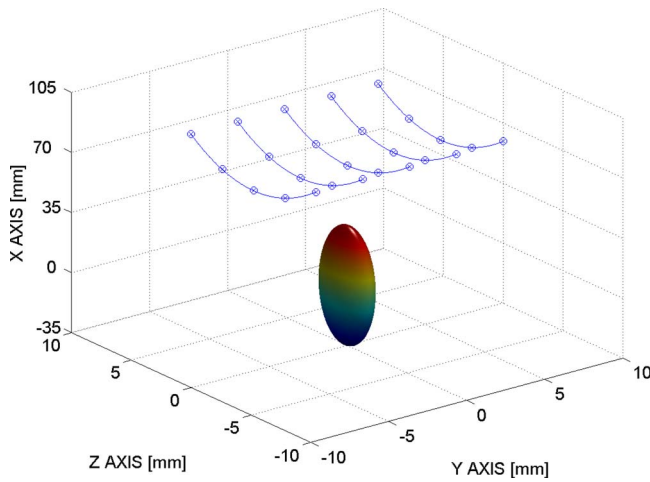


FIG. 9. (Color online) Setup for the laboratory experiment showing agar perturbation. The connected dots show the five elements of the linear array that was used to detect the lesion. The array was scanned across the ellipsoid anomaly at five different measurement locations.

with 7% Bovine Serum Albumin (BSA) protein concentration in a cylindrical container. The acoustic properties of the background phantom were: $c_b = 1540$ m/s, $\rho_b = 1045$ kg/m³, and $\alpha_b = 1.5$ Np/m/MHz.⁵⁰ The polyacrylamide hydrogel was used because it was optically transparent (allowing visualizing of the ellipsoidal anomaly), had the same density as the agar phantom, and had differences in sound speed and attenuation that were representative of a HIFU lesion. That resulted in an experiment environment of which there was a single ellipsoidal anomaly and altered sound speed and attenuation values compared to the background. A photograph of the BSA phantom showing the ellipse is given in Fig. 10. The inversion algorithm involves solving the same minimization problem as in Sec. V A, Eq. (17a). The only difference is that the transducer elements cannot be modeled as point sources. Therefore, the method described in Ref. 51 was used to compute the spatial transfer function of the cylindrical elements and incorporated into computing K_1, K_2 , and K_3 in Eq. (11). The inversion was carried out at five frequency values equally sampled between 2.5 and 3 MHz.

D. Results

The inversion was carried out using the following bounds on for the contrasts: $0 \text{ m/s} < M_c < 20 \text{ m/s}$ and

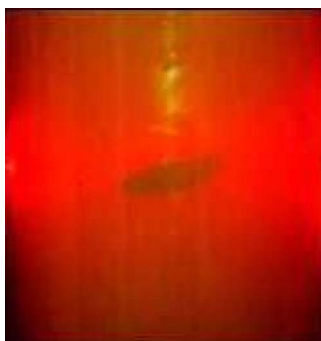


FIG. 10. (Color online) Optical image of phantom showing the ellipsoid—the dark region at the center of the image.

TABLE III. Lower and upper limits for the geometric parameters of the ellipsoid.

	Lower limit	Upper limit	Real value
x_o	−3.70 mm	0.3 mm	−1.70 mm
y_o	0 mm	4 mm	2.00 mm
z_o	−4.00 mm	3.20 mm	−2.80 mm
l_1	1.48 mm	8.30 mm	1.60 mm
l_2	0.50 mm	16.10 mm	2.60 mm
l_3	9.86 mm	12.40 mm	9.90 mm
θ_1	0.37	0.50	0.43
θ_2	0.24	0.30	0.27
θ_3	0.43	0.55	0.49

$0 \text{ Np/m} < M_a < 440 \text{ Np/m}$. Since there was no density perturbation with respect to background, M_d was set to 0. In HIFU problems, the location and orientation of the lesion can be initially estimated from the geometry of the HIFU transducer. Therefore, for this problem, it was assumed that the location and the orientation of the ellipsoid were roughly known but the lengths and contrasts were given larger bounds. The bounds for the geometric parameters used in the inversion are given in Table III.

In Fig. 11 the true ellipsoid, initial guess provided to the estimation method and the final result are displayed. For comparison purposes, the estimated ellipsoid is plotted with lines on the actual ellipsoid in Fig. 12. The number of iterations required was 116 and the total computation time was about 26 min. We were able to recover the geometry information with 5.7% volumetric estimation error. The maximum error in x , y , and z was determined to be 4.6%. The quantitative acoustic parameters of the ellipsoid is also of interest here. The initial contrast values provided to the optimization routine and the expected values are given in Table IV. Although the initial values were considerably different than the real values, we were able to determine the attenuation perturbation to within 5%. The sound speed estimate was not so accurate, with an error of 16%, however we note that the contrast in the sound speed was very small (5 m/s in 1550 m/s) and as was mentioned in Sec. I this may not be a robust parameter to determine a lesion once the lesion has cooled.

VI. CONCLUSIONS

The use of wave-based inversion methods for medical ultrasound imaging is not common. Primarily, the size of the region of interest and the limited view nature associated with most data acquisition scenarios make the traditional inversion methods, which yield complete images, impractical. However, in the case of lesions formed during HIFU the goal is to characterize objects for where there is significant prior information about the size, location, and orientation of lesions as well as their acoustic contrasts in attenuation and sound speed. Motivated by this application a shape-based method was developed for determining the acoustic properties and the spatial structure of an ellipsoidal scatterer in the Born approximation. The application of this method to HIFU-like lesions was demonstrated. This preliminary work

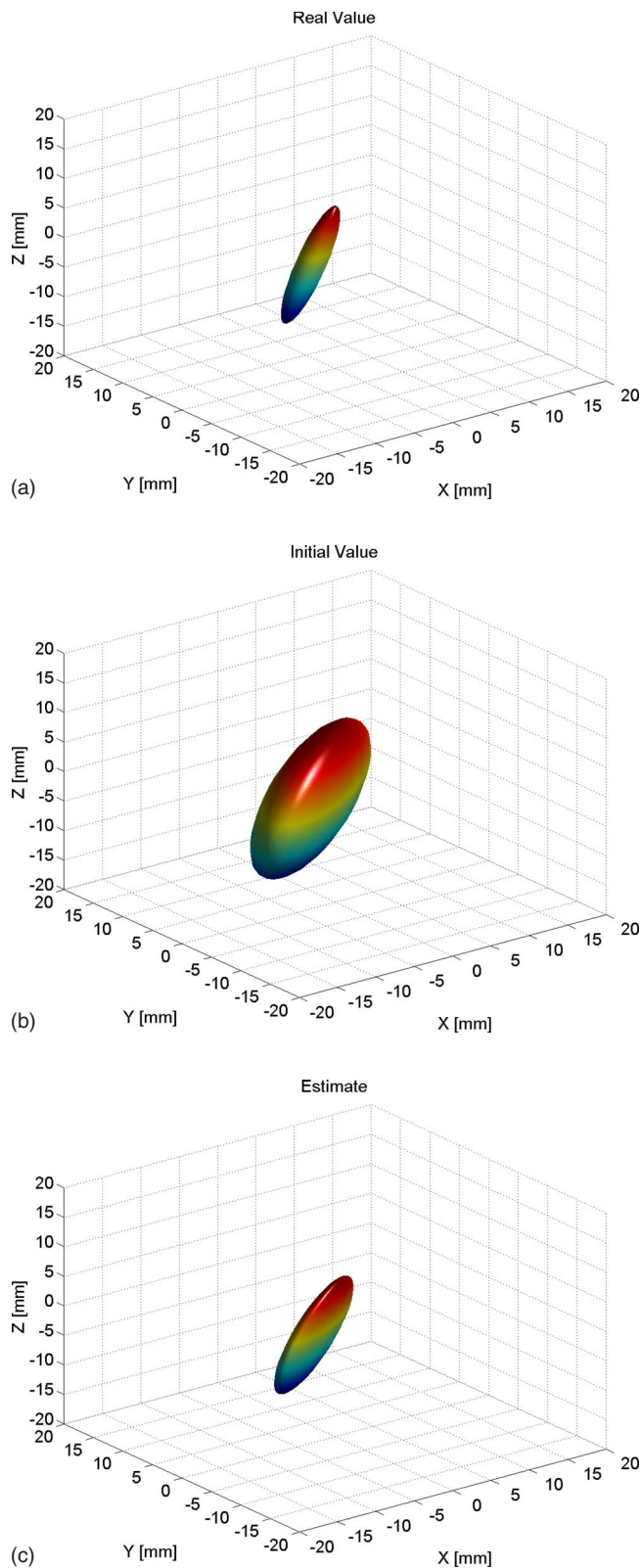


FIG. 11. (Color online) Inversion result of the experiment. The true ellipsoid (a), initial guess provided to the estimation method (b), and the final result (c) are shown.

indicates that a linearized physics-based model, coupled with a shape-based inversion routine, might provide a feasible method to monitor the progress of image guided therapy. We exploited the fact that the treatment results in an ellipsoidal-

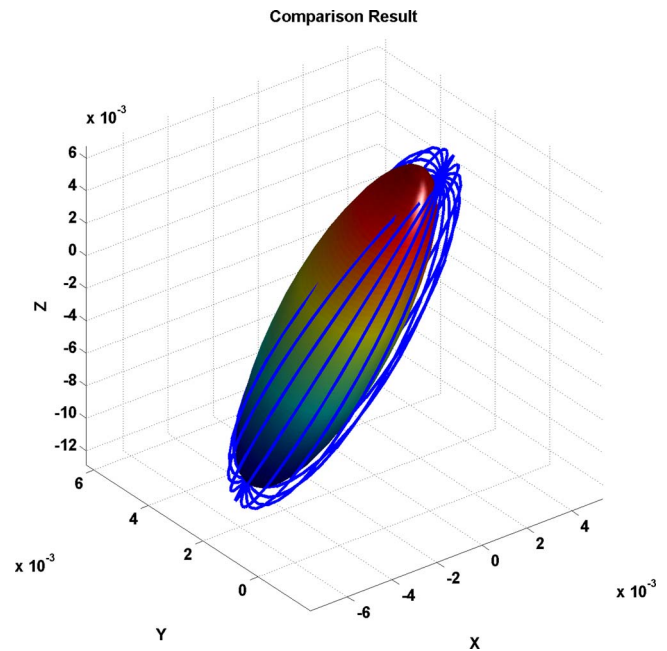


FIG. 12. (Color online) Comparison of actual and estimated ellipsoids. The estimated ellipsoid is plotted with lines on the actual ellipsoid.

shaped region and proposed a differentiable function to describe the boundary and the contrast of the ellipsoid.

Numerical simulations were used to illustrate the potential of the shape-based inversion and to show the robustness by means of a Monte Carlo approach. The Monte Carlo simulations showed that the algorithm was able to determine most of the parameters of an ellipsoid to within 10%, with the exception of the orientation angles which were found to be the hardest to accurately predict. A laboratory experiment was also considered using a clinical curvilinear array transducer. A roughly ellipsoidal HIFU lesion-like phantom was used which had perturbation in sound speed and attenuation only. We were able to reconstruct the geometry of the ellipsoid and the contrasts accurately. The results were obtained with 116 iterations using a MATLAB implementation in 26 min on a 667 MHz workstation. In practice one would need faster inversion, less than 1 min and ideally on the order of 1 s, to guide the therapy. We note that MATLAB is not an ideal computational platform to perform real-time operations. It is the experience of the authors that converting MATLAB code to a fully compiled code, using, e.g., C or FORTRAN, results in a speed up of two to three orders of magnitude. Therefore we anticipate that practical computation times will be achievable with sufficient engineering effort.

In this work we employ the Gauss–Newton method, a local optimization routine, for solving the parameter estimation problem. This method is highly sensitive to prior infor-

TABLE IV. Contrast and error values for the sound speed and attenuation.

	Real	Initial	Estimate	Err _c %	Err _v %
Sound (m/s)	5	20	5.80	16.2	5.7
Attenuation (Np/m)	48.7	440	46.3	4.9	5.7

mation particular with respect to the initial position of the ellipsoid and was motivated by the fact that for HIFU such data are readily available. With regards to the contrast parameters other experiments (not reported here) indicate that high accuracy terms of prior information are not necessary to obtain useful final results. If this technique should be applied to a case where there is no *a priori* information available, either a brute force method or global minimization technique (genetic algorithm, particle swarm, etc.) should be used to find the best initial parameters for the Gauss–Newton method as in Ref. 52.

As discussed in Sec. I, the approach we have presented is based on a number of assumptions concerning the shape of the scatterer, the nature of the medium in which it is embedded, and the physical model used in the processing. In terms of the shape assumption, the experiments in this paper indicate that accurate results can be obtained even for objects that are not perfect ellipsoids, which was indeed the case for the phantom considered in Sec. V C. Current work on this project⁵³ confirms these findings on a broader range of phantom experiments. Moving forward in making our approach more suitable for addressing the clinical form of the HIFU problem, there are many possible generalization of the ellipsoidal model which provide for the modeling of more complex shapes without the need to solve a large-scale inverse problem. We point specifically to the use of spherical harmonic expansions as the basis for modeling individual scatterers as described for example in Refs. 54–56 as well as level set methods such as those developed by Miller’s group^{57,58} and others^{59–61} for which the number of objects need not be specified *a priori*.

The method that is developed in this work is valid for homogeneous, lossy, power-law attenuating medium in which a Born scattering model is employed in the processing. Certainly, to make this approach of practical use, it will be necessary to move beyond the assumption of spatial homogeneity. Here, we must account both for fine-scale tissue inhomogeneities that give rise to typical speckle patterns in ultrasound imagery as well as large scale structures including aberrating layers, organs, etc. Our recent work⁵³ indicates a strong degree of resilience of the shape-based method for problems in which the only source of heterogeneity is the small-scale structures.

In the case of large-scale structures, many options can be explored. There are a number of approaches that have been employed to address aberration in B-mode ultrasound that could be a starting point for an inhomogeneous background model, see, e.g., Refs. 62–64. Alternatively, one could consider the use of distorted wave Born methods^{65–67} for constructing linearized models about heterogeneous media. Such an approach would allow us to easily capture large scale inhomogeneities such as the presence of organs, layers of fat, etc. Initial ideas for jointly estimating the contrast parameters when the shape of the inhomogeneities is known as well as the perturbation itself have been considered in Ref. 68. Determining the gross structure of these regions may require the acquisition and processing of, e.g., CT or MRI data prior to HIFU treatment. A major issue to be considered here is whether the lesions themselves are “small” perturba-

tions against this inhomogeneous medium. For the homogeneous problem here, the results of our work in Sec. V C indicate that for isolated lesions, the Born model is adequate. It remains to be seen whether this holds as HIFU therapy continues and produces lesions of increasing complexity. Should that not be the case then a fully nonlinear inversion routine may be needed. Here the work of Ref. 31 where an efficient contrast-source method was employed may be of use. Such techniques are well known for pixel-based image formation methods and adapting the idea for shape-based schemes would require some effort.

ACKNOWLEDGMENTS

This work was supported in part by CenSSIS (The Bernard M. Gordon Center for Subsurface Sensing and Imaging Systems), under the Engineering Research Centers Program of the National Science Foundation (Award No. EEC-9986821) the NIH under Grant No., R21 CA123253–01 and the National Science Foundation under Grant 0208548. The authors are grateful for technical assistance provided by Dr. Emmanuel Bossy and Ersel Karbeyaz.

APPENDIX: JACOBIAN CALCULATION

The Jacobian matrix associated with Eq. (12) is

$$\frac{\partial y}{\partial \mu} = -[\mathbf{K}_1 \mathbf{K}_2 \mathbf{K}_3] \begin{bmatrix} \frac{\partial \mathbf{f}_1}{\partial \mu} \\ \frac{\partial \mathbf{f}_2}{\partial \mu} \\ \frac{\partial \mathbf{f}_3}{\partial \mu} \end{bmatrix}, \quad (\text{A1})$$

where μ is the unknown geometric parameter of the ellipsoid and each \mathbf{f}_i a column vector containing the voxel values of the perturbations. To obtain the Jacobian matrix, the derivatives of Eq. (16) with respect to the unknown ellipsoid parameters are required.

Using the chain rule:

$$\frac{\partial \gamma_i(r', \beta_i)}{\partial \mu} = -10.4 \tilde{M}_i \operatorname{sech}(1.3x^8) \tanh(1.3x^8) x^7 \times \exp(\tilde{M}_i \operatorname{sech}(1.3x^8)) \frac{\partial x}{\partial \mu}, \quad (\text{A2a})$$

$$\frac{\partial \gamma_i(r', \beta_i)}{\partial M_i} = \operatorname{sech}(1.3x^8) \exp(\tilde{M}_i \operatorname{sech}(1.3x^8)), \quad (\text{A2b})$$

where $x = \|D_i U_i^T(r - c_i)\|_2^2$. Using matrix algebra x can be written as

$$x = (r' - c_i)^T U_i D_i^T D_i U_i^T (r' - c_i).$$

The derivatives of x with respect to the various ellipsoid parameters can be expressed as

$$\frac{\partial x}{\partial x_{oi}, y_{oi}, z_{oi}} = 2 \frac{\partial (r' - c_i)^T}{\partial x_{oi}, y_{oi}, z_{oi}} U_i D_i^T D_i U_i^T (r' - c_i), \quad (\text{A3a})$$

where

$$\frac{\partial(r' - c_i)}{\partial x_{oi}} = \begin{bmatrix} -1 \\ 0 \\ 0 \end{bmatrix} \frac{\partial(r' - c_i)}{\partial y_{oi}} = \begin{bmatrix} 0 \\ -1 \\ 0 \end{bmatrix} \frac{\partial(r' - c_i)}{\partial z_{oi}} = \begin{bmatrix} 0 \\ 0 \\ -1 \end{bmatrix}, \quad (\text{A3b})$$

$$\frac{\partial x}{\partial l_{1i}, l_{2i}, l_{3i}} = 2(r' - c_i)^T U_i D_i^T \frac{\partial D_i}{\partial l_{1i}, l_{2i}, l_{3i}} U_i^T (r' - c_i), \quad (\text{A4a})$$

where

$$\begin{aligned} \frac{\partial D_i}{\partial l_{1i}} &= \begin{bmatrix} -1/l_{1i}^2 & 0 & 0 \\ 0 & 0 & 0 \\ 0 & 0 & 0 \end{bmatrix}, \\ \frac{\partial D_i}{\partial l_{2i}} &= \begin{bmatrix} 0 & 0 & 0 \\ 0 & -1/l_{2i}^2 & 0 \\ 0 & 0 & 0 \end{bmatrix}, \\ \frac{\partial D_i}{\partial l_{3i}} &= \begin{bmatrix} 0 & 0 & 0 \\ 0 & 0 & 0 \\ 0 & 0 & -1/l_{3i}^2 \end{bmatrix} \end{aligned} \quad (\text{A4b})$$

and

$$\frac{\partial x}{\partial \theta_{1i}, \theta_{2i}, \theta_{3i}} = 2(r' - c_i)^T \frac{\partial U_i}{\partial \theta_{1i}, \theta_{2i}, \theta_{3i}} D_i^T U_i^T (r' - c_i), \quad (\text{A5a})$$

where

$$\frac{\partial U_i}{\partial \theta_{1i}} = \begin{bmatrix} -\sin(\theta_{1i}) & \cos(\theta_{1i}) & 0 \\ -\cos(\theta_{1i}) & -\sin(\theta_{1i}) & 0 \\ 0 & 0 & 0 \end{bmatrix} U_{2i} U_{3i}, \quad (\text{A5b})$$

$$\frac{\partial U_i}{\partial \theta_{2i}} = U_{1i} \begin{bmatrix} -\sin(\theta_{2i}) & 0 & \cos(\theta_{2i}) \\ 0 & 0 & 0 \\ -\cos(\theta_{2i}) & 0 & -\sin(\theta_{2i}) \end{bmatrix} U_{3i}, \quad (\text{A5c})$$

$$\frac{\partial U_i}{\partial \theta_{3i}} = U_{1i} U_{2i} \begin{bmatrix} -\sin(\theta_{3i}) & \cos(\theta_{3i}) & 0 \\ -\cos(\theta_{3i}) & -\sin(\theta_{3i}) & 0 \\ 0 & 0 & 0 \end{bmatrix}. \quad (\text{A5d})$$

¹L. Poissonnier, A. Gelet, J. Chapelon, R. Bouvier, O. Rouviere, C. Pangaud, D. Lyonnet, and J. Dubernard, "Results of transrectal focused ultrasound for the treatment of localized prostate cancer (120 patients with PSA <or+10 ng/ml)," *Prog. Urol.* **13**, 60–72 (2003).

²T. A. Gardner, M. O. Koch, A. Shalhav, R. Bihle, R. S. Foster, C. Steidle, I. Grunberger, A. S. M. Resnick, J. Cochran, V. Rao, and N. T. Sanghvi, "Minimally invasive treatment of benign prostatic hyperplasia with high intensity focused ultrasound using the Sonablate™ system: An updated report of phase III clinical studies conducted in the USA," *Proc. SPIE* **4609**, 107–114 (2002).

³N. T. Sanghvi, J. Syrus, R. S. Foster, R. Bihle, R. Casey, and T. Uchida, "Noninvasive surgery of prostate tissue by high intensity focused ultrasound: An updated report," *Proc. SPIE* **3907**, 194–200 (2000).

⁴S. Madersbacher, C. Kratzik, and M. Marberger, "Prostatic tissue ablation by transrectal high intensity focused ultrasound: Histological impact and clinical application," *Ultrason. Sonochem.* **4**, 175–179 (1997).

⁵K. Nakamura, S. Baba, S. Saito, M. Tachibana, and M. Murai, "High-intensity focused ultrasound energy for benign prostatic hyperplasia:

Clinical response at 6 months to treatment using sonablate 200," *J. Endourol.* **11**, 197–201 (1997).

⁶E. D. Mulligan, T. H. Lynch, D. Mulvin, D. Greene, J. M. Smith, and J. M. Fitzpatrick, "High-intensity focused ultrasound in the treatment of benign prostatic hyperplasia," *Br. J. Urol.* **79**, 177–180 (1997).

⁷C. Chaussy, S. Thuroff, F. Lacoste, and A. Gelet, "HIFU and prostate cancer: The European experience," in *Proceedings of the Second International Symposium on Therapeutic Ultrasound*, July 29–Aug. 1; Seattle, WA (2002).

⁸J. Kennedy, G. T. Haar, and D. Cranstron, "High intensity focused ultrasound: Surgery of the future?," *Br. J. Radiol.* **76**, 590–599 (2003).

⁹F. Wu, W. Chen, J. Bai, Z. Zou, Z. Wang, H. Zhu, and Z. Wang, "Pathological changes in human malignant carcinoma treated with high-intensity focused ultrasound," *Ultrason. Med. Biol.* **27**, 1099–1106 (2001).

¹⁰F. Wu, Z. Wang, W. Chen, W. Wang, Y. Gui, M. Zhang, G. Zheng, Y. Zhou, G. Xu, M. Li, C. Zhang, H. Ye, and R. Feng, "Extracorporeal high intensity focused ultrasound ablation in the treatment of 1038 patients with solid carcinomas in China: An overview," *Ultrason. Sonochem.* **11**, 149–154 (2004).

¹¹G. T. Clement, "Perspectives in clinical uses of high-intensity focused ultrasound," *Ultrasonics* **42**, 1087–1093 (2004).

¹²Z. Wang, J. Bai, F. Li, Y. Du, S. Wen, K. Hu, G. Xu, P. Ma, N. Yin, W. Chen, F. Wu, and R. Feng, "Study of a 'biological focal region' of high-intensity focused ultrasound," *Ultrason. Med. Biol.* **29**, 749–754 (2003).

¹³G. ter Haar, D. Sinnett, and I. Rivens, "High intensity focused ultrasound—A surgical technique for the treatment of discrete liver tumors," *Phys. Med. Biol.* **34**, 1743–1750 (1989).

¹⁴H. Cline, K. Hynynen, C. Hardy, R. Watkins, F. Schenck, and F. Jolesz, "MR temperature mapping of focused ultrasound surgery," *Magn. Reson. Med.* **31**, 628–636 (1994).

¹⁵N. McDannold, L. King, F. Jolesz, and K. Hynynen, "Usefulness of MR imaging-derived thermometry and dosimetry in determining the threshold for tissue damage induced by thermal surgery in rabbits," *Radiology* **216**, 517–523 (2000).

¹⁶K. Hynynen, O. Pomeroy, D. Smith, P. Huber, N. McDannold, J. Kettenbach, J. Baum, S. Singer, and F. Jolesz, "MR imaging-guided focused ultrasound surgery of fibroadenomas in the breast: A feasibility study," *Radiology* **219**, 176–185 (2001).

¹⁷J. C. Bamber and C. R. Hill, "Ultrasonic attenuation and propagation speed in mammalian tissues as a function of temperature," *Ultrason. Med. Biol.* **5**, 149–157 (1979).

¹⁸N. L. Bush, I. Rivens, G. R. ter Haar, and J. C. Bamber, "Acoustic properties of lesions generated with an ultrasound therapy system," *Ultrason. Med. Biol.* **19**, 789–801 (1993).

¹⁹C. A. Damianou, N. T. Sanghvi, F. J. Fry, and R. Maass-Moreno, "Dependence of ultrasonic attenuation and absorption in dog soft tissues on temperature and thermal dose," *J. Acoust. Soc. Am.* **102**, 628–634 (1997).

²⁰S. H. Bloch, M. R. Bailey, L. Crum, P. Kaczowski, G. Keilman, and P. Mourad, "Measurements of sound speed in excised tissue over temperature expected under high-intensity focused ultrasound conditions," *J. Acoust. Soc. Am.*, **103**(5), pp. 2868 (1998).

²¹A. E. Worthington and M. D. Sherar, "Changes in ultrasound properties of porcine kidney tissue during heating," *Ultrason. Med. Biol.* **27**, 673–682 (2001).

²²U. Techavipoo, T. Varghese, Q. Chen, T. A. Stiles, J. A. Zagzebski, and G. R. Frank, "Temperature dependence of ultrasonic propagation speed and attenuation in excised canine liver tissue measured using transmitted and reflected pulses," *J. Acoust. Soc. Am.* **116**, 2859–2865 (2004).

²³P. D. Tyr  us and C. Diederich, "Two-dimensional acoustic attenuation mapping of high-temperature interstitial ultrasound lesions," *Phys. Med. Biol.* **49**, 533–546 (2004).

²⁴C. Simon, P. VanBaren, and E. S. Ebbini, "Two-dimensional temperature estimation using diagnostic ultrasound," *IEEE Trans. Ultrason. Ferroelectr. Freq. Control* **45**, 1088–1099 (1998).

²⁵M. Pernot, M. Tanter, J. Bercoff, K. Waters, and M. Fink, "Temperature estimation using ultrasonic spatial compound imaging," *IEEE Trans. Ultrason. Ferroelectr. Freq. Control* **51**, 606–615 (2004).

²⁶L. A. S. Baker and J. C. Bamber, "Effect of dynamic receive focusing on reflex transmission imaging (RTI)," *Proc.-IEEE Ultrason. Symp.* **2**, 1581–1584 (2002).

²⁷A. Anand and P. J. Kaczowski, "Monitoring formation of high intensity focused ultrasound (HIFU) induced lesions using backscattered ultrasound," *ARLO* **5**, 88–94 (2004).

²⁸H. Zhong, M. Xi Wan, Y.-F. Jiang, and S. Pin Wang, "Monitoring imaging

- of lesions induced by high intensity focused ultrasound based on differential ultrasonic attenuation and integrated backscatter estimation," *Ultrasound Med. Biol.* **33**, 82–94 (2007).
- ²⁹N. Duric, P. Littrup, A. Babkin, D. Chambers, S. Azevedo, A. Kalinin, R. Pevzner, M. Tokarev, E. Holsapple, O. Rama, and R. Duncan, "Development of ultrasound tomography for breast imaging: Technical assessment," *Med. Phys.* **32**, 1375–1386 (2005).
 - ³⁰R. G. Pratt, L. Huang, N. Duric, and P. Littrup, "Sound-speed and attenuation imaging of breast tissue using waveform tomography of transmission ultrasound data," *Proc. SPIE* **6510**, 65104S (2007).
 - ³¹K. W. A. van Dongen and W. M. D. Wright, "A full vectorial contrast source inversion scheme for three-dimensional acoustic imaging of both compressibility and density profiles," *J. Acoust. Soc. Am.* **121**, 1538–1549 (2007).
 - ³²G. Dassios, "The inverse scattering problem for the soft ellipsoid," *J. Math. Phys.* **28**, 2858–2862 (1987).
 - ³³R. J. Lucas, "An inverse problem in low-frequency scattering by a rigid ellipsoid," *J. Acoust. Soc. Am.* **95**, 2330–2333 (1994).
 - ³⁴R. J. Lucas, "The inverse problem for scattering by an ellipsoidal boss," *J. Acoust. Soc. Am.* **97**, 2645–2650 (1995).
 - ³⁵G. Dassios and R. J. Lucas, "An inverse problem in low-frequency scattering by an ellipsoidally embossed surface," *Wave Motion* **20**, 33–39 (1994).
 - ³⁶T. S. Angell and R. E. Kleinman, "Polarizability tensors in low-frequency inverse scattering," *Radio Sci.* **22**, 1120–1126 (1987).
 - ³⁷M. E. Kilmer, E. L. Miller, A. Barbaro, and D. Boas, "Three-dimensional shape-based imaging of absorption perturbation for diffuse optical tomography," *Appl. Opt.* **42**, 3129–3144 (2003).
 - ³⁸M. Kilmer, E. L. Miller, A. Barbaro, and D. A. Boas, "3d shape-based imaging for diffuse optical tomography," *Appl. Opt.* **42**, 3129–3144 (2003).
 - ³⁹P. M. Morse and K. U. Ingard, *Theoretical Acoustics* (Princeton University Press, Princeton, NJ, 1966).
 - ⁴⁰B. U. Karbeyaz, E. L. Miller, R. O. Cleveland, and R. A. Roy, "Adaptive linearized modeling and inversion for 3d tissue characterization," *J. Acoust. Soc. Am.* **114**, 2379–2380 (2003).
 - ⁴¹B. U. Karbeyaz, "Modeling and shape based inversion for frequency domain ultrasonic monitoring of cancer treatment," Ph.D. thesis, Northeastern University, Boston, MA, 2005.
 - ⁴²J. A. Jensen, "A model for the propagation and scattering of ultrasound in tissue," *J. Acoust. Soc. Am.* **89**, 182–190 (1991).
 - ⁴³M. Arditi, F. Foster, and J. Hunt, "Transient fields of concave annular arrays," *Ultrason. Imaging* **3**, 37–61 (1981).
 - ⁴⁴E. Madsen, M. Insana, and J. A. Zagzebski, "Method of data reduction for accurate determination of acoustic backscatter coefficients," *J. Acoust. Soc. Am.* **76**, 913–923 (1984).
 - ⁴⁵T. L. Szabo, B. U. Karbeyaz, R. O. Cleveland, and E. L. Miller, "Determining the pulse-echo electromechanical characteristic of a transducer using flat plates and point targets," *J. Acoust. Soc. Am.* **116**, 90–96 (2004).
 - ⁴⁶S. J. Osher and R. P. Fedkiw, *Level Set Methods and Dynamic Implicit Surfaces* (Springer, New York, 2002).
 - ⁴⁷G. Ter Haar, "Acoustic surgery," *Phys. Today* **54**, 29–34 (2001).
 - ⁴⁸W. F. , W.-Z. Chen, J. Bai, J.-Z. Zou, Z.-L. Wang, H. Zhu, and Z.-B. Wang, "Pathological changes in human malignant carcinoma treated with high-intensity focused ultrasound," *Ultrasound Med. Biol.* **27**, 1099–1106 (2001).
 - ⁴⁹P. E. Gill, W. Murray, and M. H. Wright, *Practical optimization* (Academic, New York, 1981).
 - ⁵⁰C. Lafon, P. J. Kaczowski, S. Vaezy, M. Noble, and O. A. Sapozhnikov, "Development and characterization of an innovative synthetic tissue-mimicking material for high intensity focused ultrasound (HIFU) exposures," *Proc.-IEEE Ultrason. Symp.* **2**, 1295–1298 (2001).
 - ⁵¹B. U. Karbeyaz, E. L. Miller, and R. O. Cleveland, "Semi-analytical computation of the acoustic field of a segment of a cylindrically concave transducer in lossless and attenuating media," *J. Acoust. Soc. Am.* **121**, 1226–1237 (2007).
 - ⁵²J. Stalnaker and E. Miller, "Particle swarm optimization as an inversion tool for a nonlinear ux model," *IEEE International Geoscience and Remote Sensing Symposium, IGARSS 23-28 July 2007*, 432–435.
 - ⁵³B. Durning, R. O. Cleveland, and E. L. Miller, "Parametric study of a shape based inversion for detecting high-intensity focused ultrasound lesions," *J. Acoust. Soc. Am.* **121**, 3082 (2007).
 - ⁵⁴G. Boverman and E. L. Miller, "Estimation-theoretic algorithms and bounds for three-dimensional polar shape-based imaging in diffuse optical tomography," *Proceedings of the 2006 IEEE International Symposium on Biomedical Imaging: From Nano to Macro*, Arlington, VA, April 6–9, 1132–1135 (2006).
 - ⁵⁵G. Boverman, Q. Fang, E. Miller, D. H. Brooks, R. H. Moore, D. B. Kopans, and D. A. Boas, "Estimation and statistical bounds for three-dimensional polar shapes in diffuse optical tomography," *IEEE Trans. Med. Imaging* (in press).
 - ⁵⁶A. Zacharopoulos, S. Arridge, O. Dorn, V. Kolehmainen, and J. Sikora, "3d shape reconstruction in optical tomography using spherical harmonics and bem," *J. Electromagn. Waves Appl.* **20**, 1827–1836 (2006).
 - ⁵⁷O. Dorn, E. Miller, and C. Rappaport, "A shape reconstruction method for electromagnetic tomography using adjoint elds and level sets," *Inverse Probl.* **16**, 1119–1156 (2000).
 - ⁵⁸M. K. Ben Hadj Miled, and E. L. Miller, "A projection-based level-set approach to enhance conductivity anomaly reconstruction in electrical resistance tomography," *Inverse Probl.* **23**, 2375–2400 (2007).
 - ⁵⁹M. Soleimani, O. Dorn, and W. R. B. Lionheart, "A narrow-band level set method applied to eit in brain for cryosurgery monitoring," *IEEE Trans. Biomed. Eng.* **53**, 2257–2264 (2006).
 - ⁶⁰M. Soleimani, W. R. B. Lionheart, and O. Dorn, "Level set reconstruction of conductivity and permittivity from boundary electrical measurements using experimental data," *Inverse Probl.* **14**, 193–210 (2006).
 - ⁶¹O. Dorn and D. Lesselier, "Level set methods for inverse scattering," *Inverse Probl.* **22**, R67–R131 (2006).
 - ⁶²D.-L. Liu and R. C. Waag, "Correction of ultrasonic wavefront distortion using back-propagation and a reference waveform method for time-shift compensation," *J. Acoust. Soc. Am.* **96**, 649–660 (1994).
 - ⁶³S.-E. Masoy, T. Varslot, and B. Angelsen, "Iteration of transmit-beam aberration correction in medical ultrasound imaging," *J. Acoust. Soc. Am.* **117**, 450–461 (2005).
 - ⁶⁴N. M. Ivancevich, J. J. Dahl, G. E. Trahey, and S. W. Smith, "Phase-aberration correction with a 3-d ultrasound scanner: Feasibility study," *IEEE Trans. Ultrason. Ferroelectr. Freq. Control* **53**, 1432–1439 (2006).
 - ⁶⁵Y. Fei and A. J. Devaney, "Inverse scattering for real-valued scattering potentials," *Inverse Probl.* **21**, L7–L12 (2005).
 - ⁶⁶M. L. Dennison and A. J. Devaney, "Inverse scattering in inhomogeneous background media: II. Multi-frequency case and svd formulation," *Inverse Probl.* **20**, 1307–1324 (2004).
 - ⁶⁷A. J. Devaney and M. Dennison, "Inverse scattering in inhomogeneous background media," *Inverse Probl.* **19**, 855–870 (2003).
 - ⁶⁸G. Boverman, E. L. Miller, A. Li, Q. Zhang, T. Chaves, D. H. Brooks, and D. A. Boas, "Quantitative spectroscopic diffuse optical tomography of the breast guided by imperfect a priori structural information," *Phys. Med. Biol.* **50**, 3941–3956 (2005).